

# Numerical simulations of a horizontal axis water turbine designed for underwater mooring platforms

Wenlong Tian<sup>a,b,\*</sup>, Baowei Song<sup>a</sup>, James H. VanZwieten<sup>b</sup>, Parakram Pyakurel<sup>b</sup>, Yanjun Li<sup>c</sup>

<sup>a</sup> School of Marine Science and Technology, Northwestern Polytechnical University, 710072 Xi'an, Shaanxi, China

<sup>b</sup> Southeast National Marine Renewable Energy Center, Florida Atlantic University, 33431 Boca Raton, FL, USA

<sup>c</sup> College of Engineering, Florida Atlantic University, 33431 Boca Raton, FL, USA

Received 14 June 2015; revised 11 September 2015; accepted 19 October 2015

Available online 18 January 2016

## Abstract

In order to extend the operational life of Underwater Moored Platforms (UMPs), a horizontal axis water turbine is designed to supply energy for the UMPs. The turbine, equipped with controllable blades, can be opened to generate power and charge the UMPs in moored state. Three-dimensional Computational Fluid Dynamics (CFD) simulations are performed to study the characteristics of power, thrust and the wake of the turbine. Particularly, the effect of the installation position of the turbine is considered. Simulations are based on the Reynolds Averaged Navier-Stokes (RANS) equations and the shear stress transport  $k-\omega$  turbulent model is utilized. The numerical method is validated using existing experimental data. The simulation results show that this turbine has a maximum power coefficient of 0.327 when the turbine is installed near the tail of the UMP. The flow structure near the blade and in the wake are also discussed.

Copyright © 2016 Society of Naval Architects of Korea. Production and hosting by Elsevier B.V. This is an open access article under the CC BY-NC-ND license (<http://creativecommons.org/licenses/by-nc-nd/4.0/>).

**Keywords:** Horizontal axis water turbine; HAWT; Computational fluid dynamics; CFD; Hydrokinetic energy

## 1. Introduction

Underwater Mooring Platforms (UMPs) are a class of underwater devices that are anchored to the seabed using mooring cables. This device type can perform numerous functions, with expected performance durations typically ranging from months to years.

Common UMPs include subsurface buoys (oceanographic sensors, acoustic communication nodes, etc.), moored mines and self-mooring autonomous underwater vehicles (AUVs) (Robert, 2010). Currently, most UMPs are battery-powered and because of their finite energy supply and the uninterrupted consuming of energy by the onboard electronic devices, stored energy limitations typically limit the duration of their

installed operation. For example, the M-3 moored mine can only work for 12 months before the installed batteries runs out of power (Andrew et al., 2009). Extending the operational life of UMPs can significantly reduce the cost for missions where a sustained presence is require, because of the high costs associated with retrieving, repowering, and redeploying remote systems.

To nearly eliminate the need for redeploying UMPs due to power limitations energy can be extracted from renewable resources to recharge the batteries of these platforms. To our best knowledge, four kinds of ocean energy, including ocean surface solar energy, ocean thermal energy, ocean wave energy, and ocean current energy has been used to power ocean devices.

The Solar-powered AUVs (SAUVs) are a series of underwater vehicles powered by solar energy (Crimmins et al., 2006; Jalbert et al., 2003). The power system consists of a solar panel, microprocessor, battery gas gauge, charge controller and battery stack. These systems are designed for

\* Corresponding author.

E-mail address: [tianwenlong@mail.nwpu.edu.cn](mailto:tianwenlong@mail.nwpu.edu.cn) (W. Tian).

Peer review under responsibility of Society of Naval Architects of Korea.

long duration missions such as monitoring, surveillance and station keeping. Since these vehicles must surface for recharging it is infeasible to use this method to recharge the UMPs.

Researchers have also tried utilizing ocean thermal energy to propel underwater gliders (Webb et al., 2001). However, energy density of the ocean thermal energy is very low and the vehicle must follow saw-tooth-like trajectories that transient through a thermocline to gain enough energy. Therefore ocean thermal energy utilization is not suitable for UMPs which are expected to perform fix-point monitoring underwater.

Ocean wave energy has been used to power ocean sensor buoys (Jeannette, 2015). The Direct Drive System employs small electric generators that are directly driven via a surface buoy's wave-induced heave motion. However, motion in the water below a deep-water wave is vertically attenuated, that is, the horizontal and vertical velocities decrease with depth exponentially (Benoit, 2014). To maximize the generated power, the conversion device must be installed near the sea surface. Like the solar energy, wave energy is not suitable for providing power to most UMPs.

UMPs are often deployed where ocean currents are consistently available. The kinetic energy available in ocean current provides an ideal alternative to recharge the UMPs. Wenlong et al. designed a miniature vertical axis water turbine (VAWT) with controllable blades to generate the ocean current turbine and recharge a moored AUV (Wenlong et al., 2013). This turbine is similar in design to the Darrieus turbine when expanded. However, due to the disturbance of the hull of the AUV, the efficiency of the turbine was low and the maximum coefficient of the averaged power was found to be 0.1 (Wenlong et al., 2013).

Water turbines, which have been widely used for hydrokinetic power generation, can be classified into two categories depending on the orientation of turbine axis with regard to the water flow direction. The vertical axis water turbine (VAWT), also known as the cross-flow water turbine, rotates around an axis perpendicular to the current. Conversely, the horizontal axis water turbine (HAWT) has an axis of rotation parallel to the current direction. This type of turbine typically has a propeller-type design with two or three blades with rotational torque created by the lift generated on the blades. VAWTs are typically less efficient when compared with their horizontal counterparts, and have been shown to achieve poor performance when utilized on UMPs (Wenlong et al., 2013).

Experimental trials on HAWTs have been carried out by many researchers. Bahaj et al. (2007a,b) carried out a power and thrust coefficient study on a 0.8 m-diameter turbine in a towing tank and in a cavitation tunnel. They provided comprehensive high-quality data for the validation of numerical computations. Coiro et al. (2006) conducted towing tank experiments of a scaled model of an HAWT and provided the power and thrust curves at different water velocities. Galloway et al. (2011) studied the power and thrust performance of a 1/20th scale HAWT operating at yaw and in waves by performing towing tank experiments. Tedds et al. (2011) provided many turbine performance curves depending on the number of

blades, pitch angles, etc. Recently, Mycek et al. (2014a,b) studied the upstream turbulence intensity effect and the interaction between two turbines, with emphasis paid on the wake of the turbine.

To predict the performance of HAWT numerical methods have also been utilized. Blade element momentum methods (BEM) have been used widely for engineering design because of their low computational cost and high efficiency. During the past years, BEM method has been improved to account for three-dimensional (3D) effects by introducing new correction models such as tip loss (Shen et al., 2005), rotational flow (Burton et al., 2001) and dynamic stall (Leishaman, 1989). 3D inviscid models provide more physics of the turbine hydrodynamics than the BEM method. Current 3D inviscid models include lifting line (Epps et al., 2009), panel (Liu, 2010), and vortex-lattice (Lei et al., 2013). However, these methods neglect the viscous effects, which need to be considered to achieve the most accurate turbine performance predictions possible.

Computational fluid dynamics (CFD) simulations of the Navier–Stokes equations model fluid flows starting from first principles, and therefore inherently capture viscous effects. Comprehensive CFD simulations of horizontal axis water/wind turbines have been done. Michael et al. computed a 20 m-tidal turbine at different flow velocities using the commercial CFD code STAR CCM+ to investigate the effect of grid density and time step on the calculated torque (Michael et al., 2011). Monier et al. (2013) designed and optimized a winglet for the NREL Phase VI turbine using the Fine/Turbo of the commercial CFD code NUMECA. They provided a detailed CFD validation study of the NREL Phase VI turbine (Hand et al., 2001) showing that the CFD results were in good agreement with the experiment results. Yuwei et al. (2012) carried out CFD simulations of the NREL Phase VI turbine with both unsteady Reynolds-Averaged Navier–Stokes (RANS) and Detached Eddy Simulation (DES) methods. Tongchitpakdee et al. (2005) studied the aerodynamic performance of the NREL Phase VI horizontal axis wind turbine under yawed flow conditions. More recently, Nak et al. (2015) studied the effect of the distance between dual rotors on the performance and efficiency of a counter-rotating tidal turbine using both CFD and experimental methods.

In order to improve the poor power performance of the previous turbine design used for UMPs (Wenlong et al., 2013), a HAWT has been designed that can be installed on UMPs. This paper focuses on the CFD simulations of this turbine design. The study is performed using the finite volume code FLUENT 13.0 with a Rotating Reference Frame (RRM) model. The effect of the installation position on the output performance of the turbine is studied over a range of tip speed ratios (TSRs).

## 2. Description of the HAWT

The UMP considered in this study is a self-mooring AUV. The self-mooring AUV is expected to travel to a desired mooring location, moor itself on the seafloor, collect

oceanographic data for a designed period of time, and then release the mooring cable and return to a desired egress location (Robert, 2010). The UMP used in this paper is a prototype designed in Northwestern Polytechnical University, which has a maximum diameter of  $D_A = 0.5$  m and length of  $L = 7$  m (not including the propeller).

The HAWT designed for the UMP is mainly composed of three blades, three sets of leadscrew mechanism, and a Permanent Magnet (PM) generator that contains a PM rotor and a PM stator. The leadscrew mechanism is driven by a servo motor and works to control the blade, as is shown in Fig. 1(a). The blade can be opened or closed by controlling the rotation direction of the servo motor, using the motion principle of the slider crank mechanism. The PM stator is fixed on the central axis of the UMP, while the other parts, including the PM rotor, the blades, the servo motors and the leadscrew mechanisms, are installed together and rotate about the axis of the PM stator. When the blades are opened, the turbine is similar to a HAWT and uses the lift on the blades to propel the PM rotor. When they are closed, the blades fit closely to the grooves on the hull of the UMP without influencing other functions of the UMP.

Fig. 1(b) shows the case when the HAWT is mounted on the UMP. When the vehicle successfully moors to the sea floor the servo motors inside the HAWT start to work and open the blades. At the same time a heavy bar stretches from the hull of the UMP, which serves to lower the center of gravity of the UMP and resist the roll torque caused by the turbine. When moored, the HAWT works to provide sustaining energy for the vehicle, enabling the UMP to extend the moored operational time. At the end of the mooring stage, the servo motors rotate reversely and close the blades, and then the vehicle releases the mooring cable and returns to a desired egress location.

The turbine considered in this paper was designed using a BEM theory based approach. The turbine has a radius of  $R = 0.75$  m and a hub radius of 0.25 m (the radius of the UMP hull). The turbine was optimized for an inflow velocity of  $U = 0.5$  m/s and a tip speed ratio of  $TSR = 5$ . Tip speed ratio denotes the ratio between rotor blade tip speed and inflow velocity and is defined as

$$TSR = \frac{\omega R}{U}. \quad (1)$$

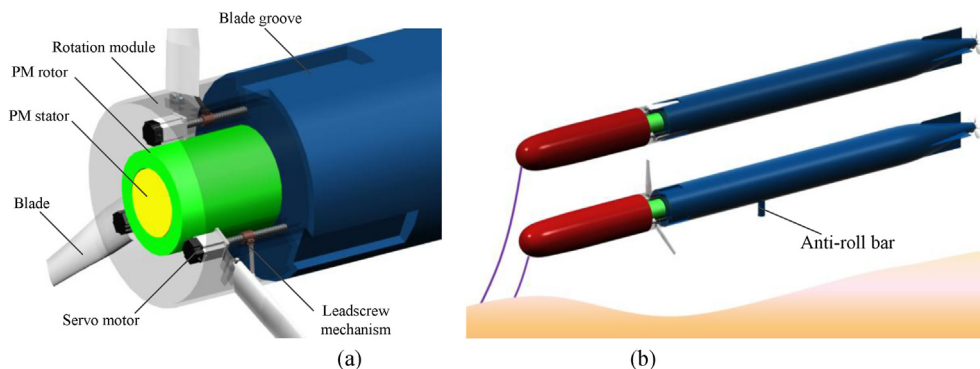


Fig. 1. The HAWT: (a) internal structure and (b) schematic of the turbine installed on an UMP.

Table 1  
Specification of the blade.

$r/R$	$c/R$	$\theta$ (deg)	$t/c$ (%)
0.4	0.1600	10.0000	25
0.5	0.1600	10.0000	18
0.6	0.1433	7.5431	18
0.7	0.1266	5.6442	18
0.8	0.1133	4.1796	18
0.9	0.1025	3.0168	18
1	0.0935	2.0717	18

NACA 63-4XX airfoils were chosen as the profile of the turbine. The NACA 63-4XX airfoils have relatively large minimum pressure coefficient and are resistant to cavitation. The blade starts from 40% span (from the rotor center to the blade tip). The thickness ratio (thickness/cord) of the blade is 25% at 40% span and decreases linearly to 18% at 50% span. Outboard of the 50% span the blade thickness is constant at 18%. Table 1 summarizes the specifications of the blade and shows the local radial position  $r$ , chord length  $c$ , twist angle  $\theta$ , and blade thickness  $t$ . It should be noted that the maximum chord length and twist angle were restricted to 0.16R and  $10^\circ$ , respectively. The main consideration was that the blade cannot fit to the hull of the UMP if the chord length and twist angle are too large. In order to minimize the blade actuating force, the location of the blade pivot point was determined at a 25% chord from the leading edge, which is the hydrodynamic center.

While the geometric parameters of the turbine were known, the installation position of the turbine needed to be determined (Fig. 2). Unlike typical HAWTs with a relatively small hub, the turbine in this paper has a much smaller size when compared with the UMP body. Therefore, the UMP body inevitably affects the performance of the turbine. Five installation positions,  $l = 0.2L$ ,  $l = 0.4L$ ,  $l = 0.6L$ ,  $l = 0.7L$  and  $l = 0.8L$  were considered and compared in the CFD simulations, with locations referring to the distance behind the front of the UMP. Further, to study the effect of the rudders, two more cases are evaluated without rudders ( $l = 0.4L$  and  $l = 0.7L$ ). To simplify the simulation and reduce the number of grid elements, the UMP propeller is neglected in the simulations. Table 2 lists the cases in the simulations.

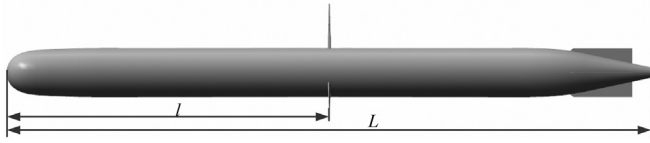


Fig. 2. Illustration of the installation position of the turbine.

Table 2  
Simulation cases.

Case	$l/L$	Other
1	0.2	With rudders
2	0.4	With rudders
3	0.6	With rudders
4	0.7	With rudders
5	0.8	With rudders
6	0.4	Without rudders
7	0.7	Without rudders

### 3. Numerical method

The commercial CFD code FLUENT v13.0 was used to solve the incompressible RANS equations using a second-order-accurate finite-volume discretization scheme. The shear stress transport (SST)  $k-\omega$  turbulence model was selected to model the turbulence terms of the RANS equations. The SST  $k-\omega$  turbulence model is able to model the transport of turbulent shear stress, gives accurate predictions on the onset and amount of flow separation under adverse pressure gradients, and has been successfully used in the CFD simulation of wind/water turbines (Michael et al., 2011; Nak et al., 2015).

A rotating reference frame model was used to simulate the rotation of the rotor for the economy of computation time. This method simulates the rotation of the rotor without physically rotating the grid by forming the governing equations for the rotor domain in a reference frame that rotates with the turbine, while the outer domain remains in a stationary coordinate system (Michael et al., 2011).

#### 3.1. Computation domains and boundary conditions

In this simulation the computational domain was sized to allow for full development of the upstream flow and to minimize blockage effects. The computation domain is a cylinder with a radius of  $8R$  and a stream wise length of  $5.5L$  ( $25.67D$ ). The UMP was placed in the centerline of the cylinder and at a distance of  $3L$  ( $14D$ ) from the downstream boundary. Fig. 3 shows the dimension of the domain and the topology of the grid. Several previous studies only simulated one blade of the turbine considering the periodicity of the rotor (Michael et al., 2011; Monier et al., 2013; Tongchitpakdee et al., 2005; Nak et al., 2015). However, the UMP in this study has three blades and four rudders and therefore it is not sufficient to simulate only one blade.

The overall domain was split into three subdomains. The first one contains the grid elements surrounding the rotor (referred to as the rotor domain). The second one contains the cells surrounding the tail of the UMP (referred to as the tail domain). The last one is the outer domain containing the cells in the outer region. The split of the tail from the UMP is mainly to simplify the generation of the grids.

A uniform and steady velocity profile of  $0.5$  m/s was applied at the inlet of the computation domain. It is known that turbulence intensity plays an important role on the behaviour of a HAWT. The mean performances, like torque and thrust, are hardly influenced by this parameter but the performance fluctuations dramatically increase with the turbulence intensity. The wake dissipates much faster as the turbulence intensity increases (Mycek et al., 2014a). As this paper focuses on the influence of turbine positions, the effect of turbulence intensity is ignored and a uniform turbulence intensity of  $1\%$  was set and modeled at the inlet.

A pressure outlet boundary was applied at the outlet of the domain. To improve the stability of the numerical simulations, symmetry boundary conditions were applied at the side wall of the cylinder. The symmetry boundary condition is useful because it allows the solver to consider the wall as part of a larger domain, avoiding the wall effects. No-slip boundary

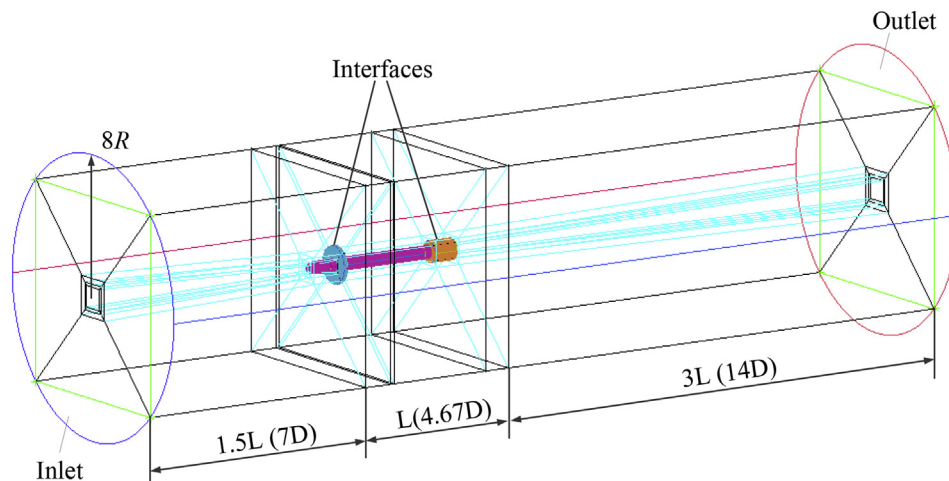


Fig. 3. Computation domains.

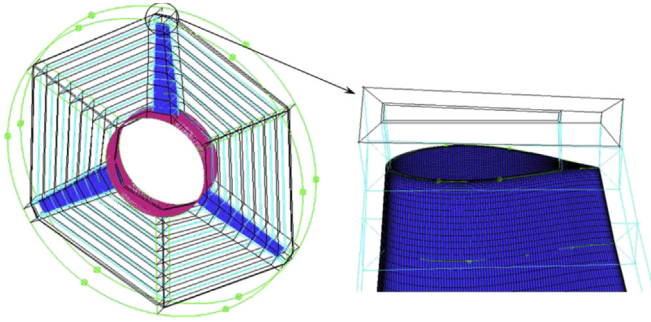


Fig. 4. Grid of the rotor subdomain.

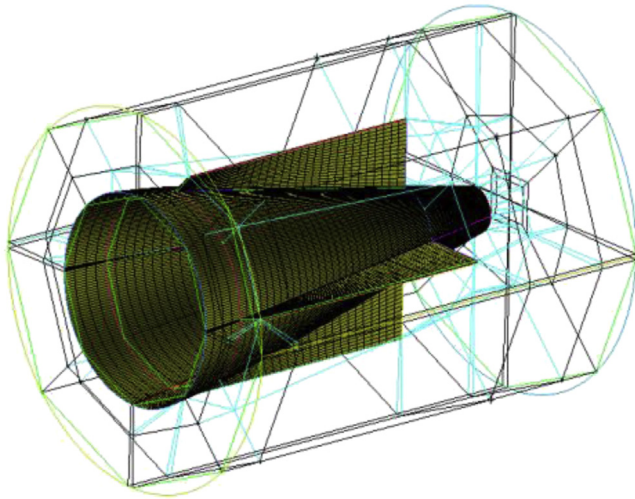


Fig. 5. Grid of the tail subdomain.

conditions were imposed at the surface of the blades and the hull of the UMP. Two interfaces were imposed at the overlap faces between the adjacent subdomains, allowing the transport of the flow properties.

### 3.2. Grid generation

The fidelity of any CFD simulations depends on the type of grid utilized (e. g. structured or unstructured) with the structured hexahedral grids being most desirable because they inherently provide highly accurate numerical solutions (Michael et al., 2011). In the present study, all structured grids were generated using the ICEM grid generation utility in ANSYS 13.0. The grids of the three subdomains were

generated separately and then merged together. The grid nodes density was higher in the rotor domain than in the other domains. The grid behind the rotor and near the hull of the UMP, where high velocity gradients were expected, was refined with a higher grid resolution. Prism layer grid elements were extruded from the surfaces of the blade to improve the grid quality and describe with sufficient precision the boundary layer flow. The height of the first prism layer above the surface was set so that the  $y^+$  value for the first elements from the wall was below 1, depending on the rotation velocity of the rotor and the position of the elements on the blade. This  $y^+$  value made it ideal for the use SST  $k - \omega$  turbulence model. A mesh growth rate of 1.2 was chosen for all subdomains.

Figs. 4 and 5 shows the topology of the grids in the rotor subdomain and the tail subdomain. Three grids were generated for the grid resolution study. The main difference of these grids is the grid resolution on the blades and behind the rotor.

### 3.3. Solution sets

For each case listed in Table 1, multiple simulations were carried out for tip speed ratios ranging from 2 to 7. Convergence was determined by the order of magnitude of the residuals. The drop of all scaled residuals below  $1 \times 10^{-5}$  was employed as convergence criterion. The maximum number of iterations was set as 2000, which enabled all the residuals to meet convergence in the simulation. The coupled pressure–velocity coupling method was used in all simulations. A Second Order Upwind spatial discretization algorithm was used for all the equations, including pressure, momentum and turbulence, and a Least Squares Cell Based algorithm was used for the gradients. The second order algorithms give more accurate results than first order ones because they reduce interpolation errors and false numerical diffusion.

## 4. Numerical method verification and validation

### 4.1. Verification

A grid resolution study and domain size study were performed to evaluate the influence of grid resolution and domain size on the torque of the rotor. The simulations were conducted on the case 1 turbine in Table 2 at a TSR of 5. Table 3 summarizes the calculated torques with different grid resolutions and domain sizes. It can be seen from the first three results that grids with approximately  $8.2E+06$  and  $1.1E+07$  elements gave approximately the same results. This indicates that further increasing the grid resolution would not significantly affect the rotor torque predicted by CFD simulations. No. 4 has the same grid resolution with No. 2 but a larger domain, with a radius of  $16R$ . The difference is considerably small between the torques obtained from these two cases. This means that the blockage effect caused by the boundaries of the domain can be ignored when the radius of the domain is larger than  $8R$ . Considering the economy of time in the simulation, the grid with  $8.2E+06$  elements and the domain with  $8R$  were chosen for the following simulations.

Table 3  
Calculated torque when  $l = 0.2 L$  and  $TSR = 5$ .

Number	Radius of the domain	Approx. number of grid elements	Torque/Nm
1	$8R$	$6.3E+06$	10.76
2	$8R$	$8.2E+06$	10.69
3	$8R$	$1.1E+07$	10.66
4	$16R$	$10.3 E+06$	10.67

Table 4  
Setting for the simulation verification.

Parameters	Value
Number of blades	3
Blade section	NACA63-8XX
Diameter of the turbine	0.8 m
Inflow velocity	1.73 m/s
TSR	5–10

where  $P$  is the generated power. It can be observed that the CFD results are in good agreement with the experimental results, especially at higher tip speed ratios. The maximum relative error occurs at  $TSR = 5$ , where the CFD result is about 8% lower than the experiment data. This means that the numerical method in the present study will likely minimally under-predict the power absorbed by this system.

5. Results and discussion

5.1. Torque and power characteristics

Fig. 7(a) depicts the curves of power coefficient for different turbine installation positions. Considering the five cases where the rudder is modeled, it can be seen that all the curves, except for  $l = 0.4L$ , show the same trend over the tested tip speed ratios. All cases have a same minimum  $C_p$  value of approximately 0.03 at  $TSR = 2$  where the blades of the rotor are in deep stall. The  $C_p$  curves increase with  $TSR$  and reach their peak at  $TSR = 5$ , before decreasing sharply beyond  $TSR = 6$ . While for the case of  $l = 0.4L$ , the  $C_p$  curve is lower than the other four cases and reaches its peak at  $TSR = 6$ . As  $TSR$  further increases, the  $C_p$  curve drops smoothly and is almost twice as large as the other four cases.

The loss of power for  $l = 0.4L$  for TSRs of 4 and 5 is caused by the increased turbulence intensity upstream from the rotor. The separated flow from the nose of the UMP grows in the axial direction, and the turbulence intensity increases as well. Fig. 8 shows the contours of turbulence intensity in the cross-sectional planes, which are perpendicular to the axis of the UMP and locates at 0.1R upstream of the rotors. In Fig. 8 the increase of turbulence intensity near the roots of the rotors is clearly shown. It is known that a higher turbulence intensity leads to lower coefficient of power (Mycek et al., 2014a,b).

For TSRs of 4 and 5, the  $C_p$  values for  $l = 0.6L$ ,  $l = 0.7L$  and  $l = 0.8L$  didn't drop like  $l = 0.4L$ , though even higher turbulence intensity were seen. An explanation for this is that the turbines in these cases are closer to the rudders and rudders work like rectifying plates, reducing the rotating flow in the wake and making the turbine very robust to turbulent upstream velocity conditions. Two more cases,  $l = 0.4L$  without rudder (case 6) and  $l = 0.7L$  without rudder (case 7) were used to

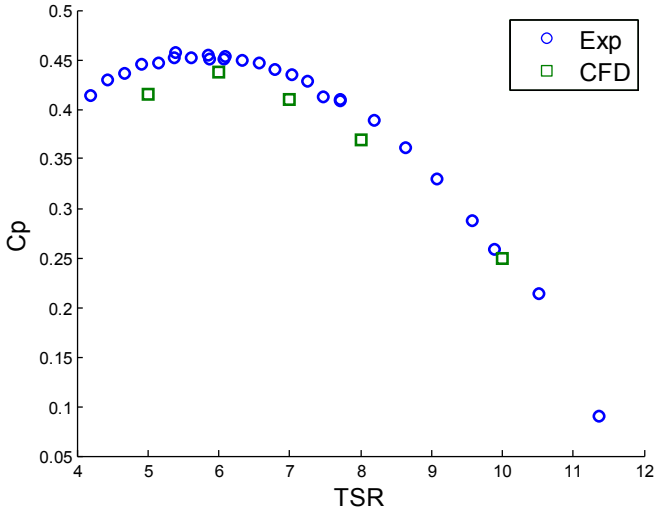


Fig. 6. Results of the numerical method validation.

4.2. Validation

In order to validate the accuracy of the method used in this paper, CFD simulations were performed on the HAWT in Bahaj et al. (2007a,b). The numerical results are then compared with the cavitation tunnel experimental data from Bahaj et al. (2007a,b). The setting of the experimental model is listed in Table 4. Fig. 6 shows the comparison of the coefficient of power between CFD and experimental data at a range of TSRs. The coefficient of power is defined as

$$C_p = \frac{P}{0.5\rho\pi R^2 U^3}, \tag{2}$$

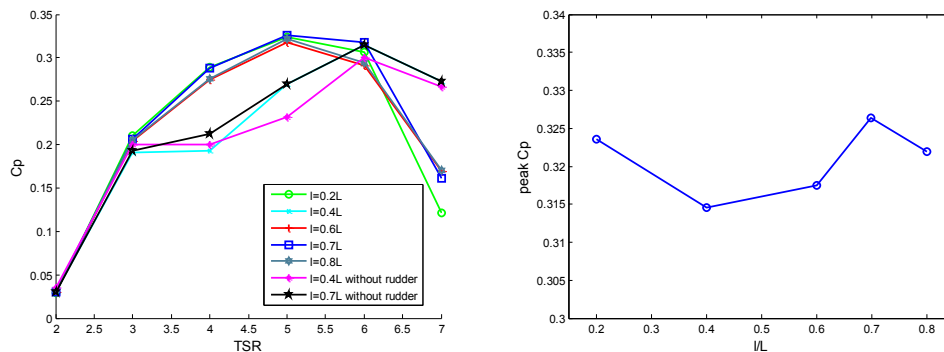


Fig. 7. The results of  $C_p$ : (a)  $C_p$  vs  $TSR$  and (b) peak  $C_p$  vs  $l$ .

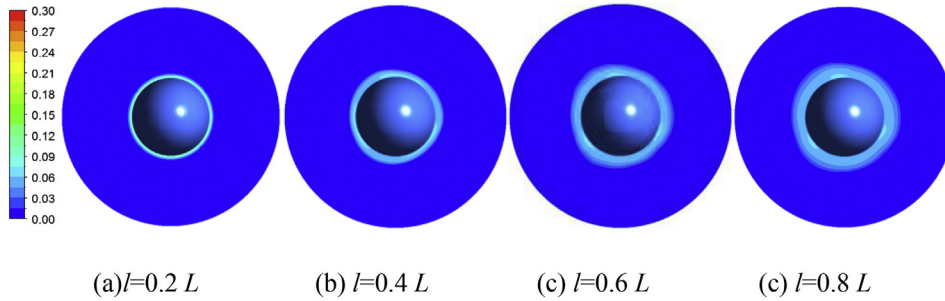


Fig. 8. Contours of turbulence intensity at the cross-sectional planes  $0.1R$  upstream of the turbines of  $l = 0.2L, 0.4L, 0.6L$  and  $0.8L$  at  $TSR = 5$ .

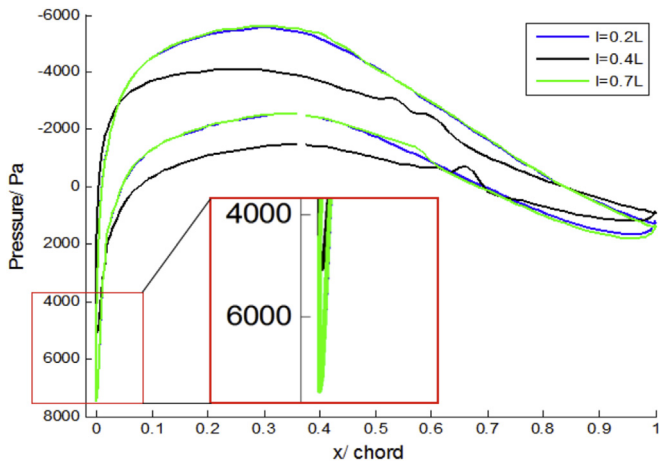


Fig. 9. Pressure distribution on 90% span sections at  $TSR = 7$ .

support this explanation. Comparing the  $C_p$  curves of  $l = 0.4L$  and  $l = 0.4L$  without rudder in Fig. 7, we find no much difference and can say that rudder effect was hardly felt by the turbine at  $l = 0.4L$ . Comparing the  $C_p$  curves of  $l = 0.7L$  and  $l = 0.7L$  without rudder in Fig. 7, we find that the  $C_p$  is obviously increased due to the rudder effect. This finding is an

important guide for the installation of turbines on AUV-like UMPs, we should either place the turbine near the nose where the turbulence intensity is small or near the tail where rudder effect is strong.

The relatively high  $C_p$  of  $l = 0.4L$  at  $TSR = 7$  can be explained with the pressure distribution in Fig. 9. Fig. 9 shows the pressure distribution on the 90% span sections at  $TSR = 7$ . The cases of  $l = 0.4L$  generates higher pressure on both the pressure and the suction side of the blade than that of  $l = 0.2L$  and  $l = 0.7L$ , but the difference of the net pressure is small. Another finding is that the maximum pressure near the leading edge ( $x/c$  near zero) of the cases  $l = 0.2L$  and  $l = 0.7L$  is almost 2500 Pa larger than cases of  $l = 0.4L$ . The higher pressure at the leading edge will inevitably generate larger drag and thus reduce the torque and eventually power.

Fig. 7(b) shows the variation of the peak  $C_p$  values with respect to  $l$ . The maximum  $C_p$  is obtained in the case of  $l = 0.7L$  at  $TSR = 5$ , with a value of 0.327. This value is considerably higher than a previous VAWT for UMPs, which is only 0.10 (Wenlong et al., 2013). The  $C_p$  of  $l = 0.2L$  and  $l = 0.8L$  is slightly smaller than  $l = 0.7L$ . The case of  $l = 0.4L$  has the smallest peak  $C_p$ , 0.315.

Fig. 10 depicts the curves of thrust coefficient for different turbine installation positions. It can be seen that the coefficient of thrust increases with tip speed ratio in the tested region of tip speed ratios. The thrust evolution of the turbine also presents a similar behavior to that of the power curve: the  $C_t$  of  $l = 0.2L, 0.6L, 0.7L$  and  $0.8L$  has the same trend while the  $C_t$  of  $l = 0.4L, 0.4L$  without rudder and  $0.7L$  without rudder are close. Generally, the coefficient of thrust for the cases of  $l = 0.2L, 0.6L, 0.7L$  and  $0.8L$  are higher than the other cases when  $TSR > 3$ . This is also caused by the increased turbulence intensity. Previous study has proved that higher turbulence intensity will result in smaller coefficient of thrust (Mycek et al. 2014a,b).

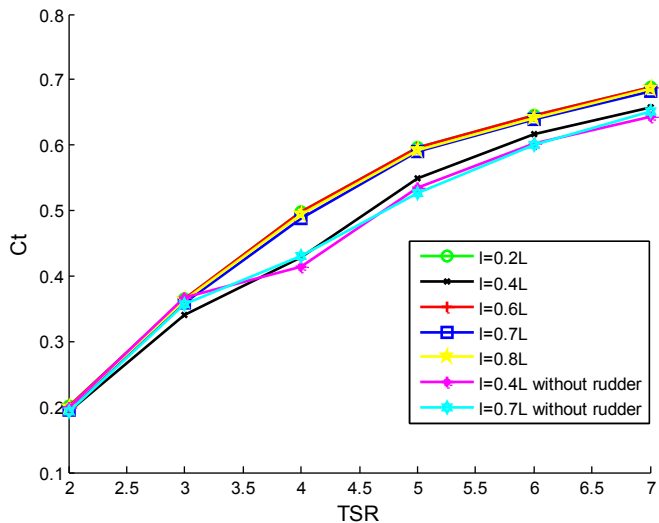


Fig. 10. The coefficient of thrust against tip speed ratios.

### 5.2. Flow near the blade

Fig. 11 presents the pressure distribution and limiting streamlines on both the pressure and the suction side of the blade for case 1, 2 and 4. These three cases were chosen because of their representative positions, nose, middle and tail. At low tip speed ratio ( $TSR = 2$ ) fully attached flow is observed on most of the pressure surface of the blade, except

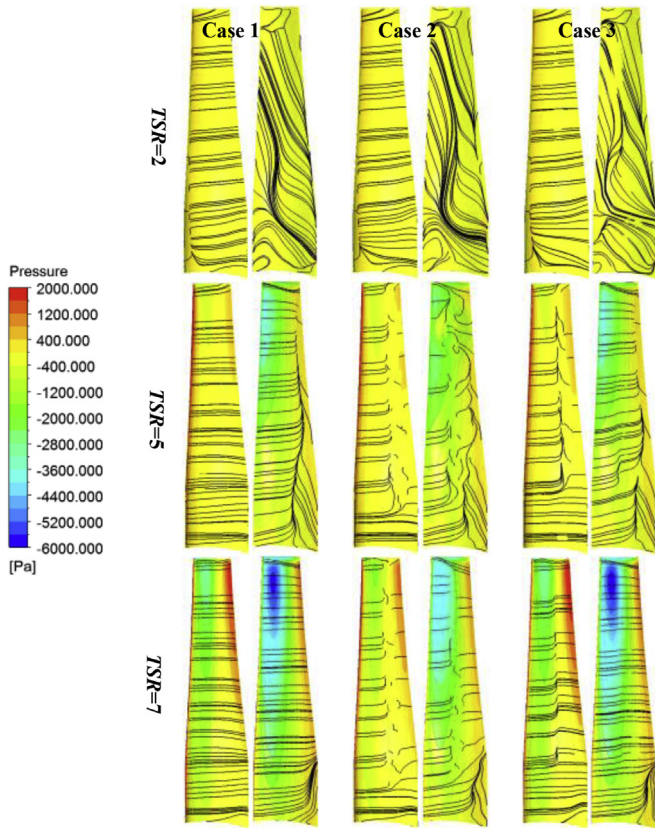


Fig. 11. Blade pressure distribution and limiting streamlines on both side of the blade at different tip speed ratios.

for the root area. Significant separation flow is observed on the whole suction side of the blade. Fig. 12 shows the streamlines and contours of pressure on the selected sections at  $TSR = 2$ . The separation flow can be seen clearly at all sections with unsteady shedded vortices. At 50% span and 90% span the flow separates from the leading edge and reattaches to the suction surface of the blade. At 70% span the flow separates from both the leading edge and the trailing edge and forms two contra-rotating vortices. Comparing the cases at  $TSR = 5$  and  $TSR = 7$ , significant pressure recovery is observed on the suction surface due to the shedding of the vortices.

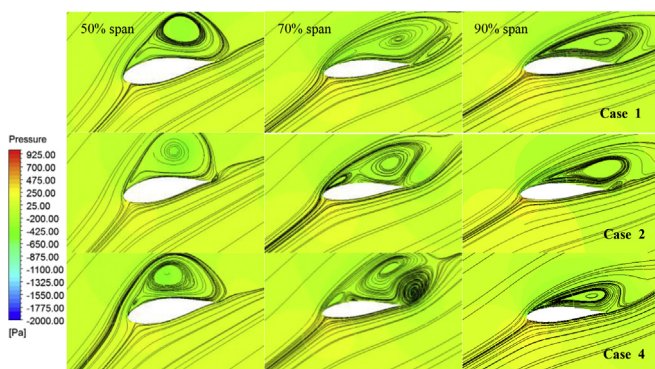


Fig. 12. Streamlines and contours of pressure on the selected sections at  $TSR = 2$ .

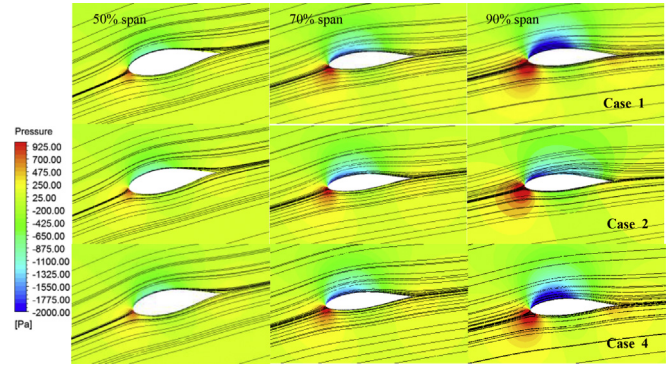


Fig. 13. Streamlines and contours of pressure on the selected sections at  $TSR = 5$ .

At  $TSR = 5$  and on the pressure surface only case 1 ( $l = 0.2L$ ) predicts fully attached flow. While for the other three cases, radial flow is observed beyond 50% span and at about 50% chord position. On the suction side slight flow separation, which starts from the root and near to the trailing edge (about 80% chord) is observed in all cases. But note that the flow before the separation point is more turbulent in case 2 ( $l = 0.4L$ ), which leads to a pressure recovery on the suction surface. This can also be observed in Fig. 13, which shows detailed streamlines and pressure contours on the selected sections.

At  $TSR = 7$  and on the pressure surface the limiting streamlines shows a similar trend to that of  $TSR = 5$ . But on the suction side both case 1 ( $l = 0.2L$ ) and case 4 ( $l = 0.7L$ ) predict fully attached flow on the whole surface except for a small area near the root. While for case 2 ( $l = 0.4L$ ) though attached flow is observed, a radial flow is also seen at about 50% chord position. Fig. 14 shows the streamlines and contours of pressure on the selected sections at  $TSR = 7$ . Due to the increased inflow velocity and reduced angle of attack, the positive pressure at the leading edge and the trailing edge is increased when compared with Figs. 11 and 12 and the negative pressure on the sides of the blade changes on the opposite.

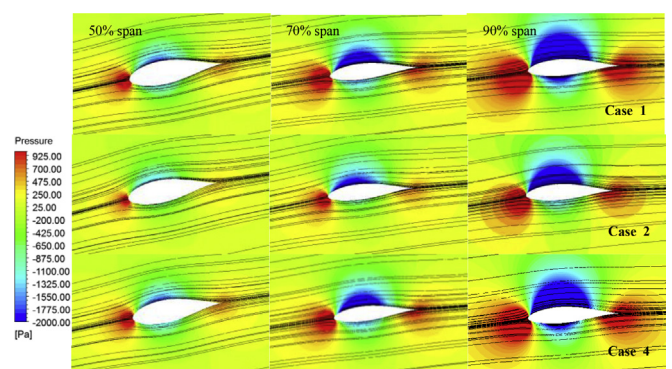


Fig. 14. Streamlines and contours of pressure on the selected sections at  $TSR = 7$ .

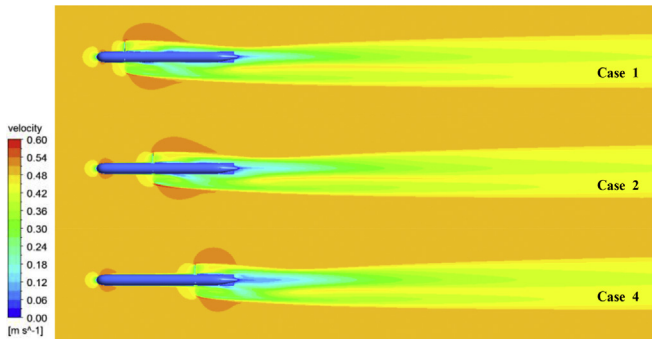


Fig. 15. Contours of velocity at the lateral cross-section planes at  $TSR = 5$ .

### 5.3. Wake properties

Fig. 15 presents two-dimensional contours of axial velocity at the lateral cross-section planes for case 1, 2 and 4 at  $TSR = 5$ . The upstream fluid is slowed when it passes the turbine and forms a low-velocity zone behind the turbine. This low-velocity zone extends to up about  $6D$  downstream of the turbine for all cases regardless of the installation position of the turbine. A small high-velocity zone is observed outside the tip of the blade in the downstream direction. This high-velocity zone is almost the same size in case 1 and case 2, and is larger than in case 4. There is no significant difference in the far wakes of the four cases. The velocity is disturbed in a limited axial strip, which enlarges smoothly along the flow direction and becomes about  $1.8D$  large at  $3L$  downstream of the UMP. The axial velocity at the  $3L$  downstream of the UMP recovers to about 90% of the inflow velocity.

## 6. Conclusion

In this study a horizontal axis water turbine designed for UMPs was presented. Three-dimensional CFD simulations were performed on this type of turbine. After the verification and validation of the numerical method, the effect of the installation position on the turbine performance was studied. The following conclusions were drawn:

- 1) The case of  $l = 0.7L$  has the maximum  $C_p$  of 0.327, which is obtained at  $TSR = 5$  (the design  $TSR$  of the rotor) and more than three times larger than that of a VAWT previously designed for UMPs.
- 2) The rudders can make the turbine robust to turbulent upstream velocity conditions.
- 3) All cases have similar wakes. The axial velocity in the wake is disturbed in a limited axial strip, which enlarges along the flow direction and becomes about  $1.8D$  large at  $3L$  downstream from the UMP.

In this research, the turbine was modeled as rotating about a fixed axis and the movement of the UMP was ignored. Future work will focus on the interaction between the turbine and the UMP, as well as the performance of the turbine at yaw conditions.

## Acknowledgement

This research was supported by the National Science Foundation of China (Grant No. 51179159) and the Doctorate Foundation of Northwestern Polytechnical University (CX201307). The authors would also like to thank the support of the High Performance Computing center at Florida Atlantic University.

## References

- Andrew, E., Lyle, G., William, M., 2009. Chinese Mine Warfare—a PLA Navy ‘Assassin’s Mace’ Capability. US Naval War College, Rhode Island.
- Bahaj, A., Molland, A., Chaplin, J., Batten, W., 2007a. Power and thrust measurements of marine current turbines under various hydrodynamic flow conditions in a cavitation tunnel and a towing tank. *Renew. Energy* 32, 407–426.
- Bahaj, A., Batten, W., McCann, G., 2007b. Experimental verifications of numerical predictions for the hydrodynamic performance of horizontal axis marine current turbines. *Renew. Energy* 32, 2479–2490.
- Benoit, C., 2014. *Environmental Fluid Mechanics*. John Wiley & Sons, Inc.
- Burton, T., Sharpe, D., Jenkins, N., Bossanyi, E., 2001. *Wind Energy Handbook*. John Wiley & Sons Ltd.
- Crimmins, M., Patty, T., Beliard, A., et al., 2006. Long endurance test results of the solar-powered AUV system. In: *OCEANS 2006*, pp. 1–5. Boston, MA.
- Coiro, P., Maisto, U., Scherillo, F., et al., 2006. Horizontal axis tidal current turbine: numerical and experimental investigations. In: *Owemes 2006*. Civitavecchia, Italy.
- Epps, P., Stanway, J., Kimball, W., 2009. An open-source design tool for propellers and turbines. In: *Society of Naval Architects and Marine Engineers Propeller/Shafting ’09 Symposium*, Williamsburg, VA.
- Galloway, P., Myers, L., Bahaj, A., 2011. Experimental and numerical results of rotor power and thrust of a tidal turbine operating at yaw and in waves. In: *World Renewable Energy Congress 2011*, pp. 2246–2253. Linköping, Sweden.
- Hand, M., Simms, D., Fingersh, L., et al., 2001. Unsteady Aerodynamics Experiment Phase VI: Wind Tunnel Test Configurations and Available Data Campaigns. NREL/TP-500–29955, Colorado.
- Jalbert, J., Baker, J., Duchesney, J., et al., 2003. A solar-powered autonomous underwater vehicle. In: *OCEANS 2003*, pp. 1132–1140. San Diego, CA.
- Jeannette, G., 2015. Wave Energy Conversion Systems Designed for Sensor Buoys. Available: [http://www.electrostandards.com/images/user/File/WaveEnergyConversionSystems\\_5294-01ee.pdf](http://www.electrostandards.com/images/user/File/WaveEnergyConversionSystems_5294-01ee.pdf). (accessed 25.05.15.).
- Lei, H., Spyros, A., Kinnas, A., 2013. Vortex-lattice method for the prediction of unsteady performance of marine propellers and current turbines. *Int. J. Offshore Polar Eng.* 23, 210–217.
- Leishaman, G., 1989. A semi-empirical model for dynamic stall. *J. Am. Helicopter Soc.* 34, 3–17.
- Liu, P., 2010. A computational hydrodynamics method for horizontal axis turbine-Panel method modeling migration from propulsion to turbine energy. *Energy* 35, 2843–2851.
- Michael, L., Ye, L., Danny, S., 2011. Development and verification of a computational fluid dynamics model of a horizontal-axis tidal current turbine. In: *30th International Conference on Ocean, Offshore, and Arctic Engineering*, Rotterdam, Netherlands.
- Monier, E., Nilay, S., Sinan, A., 2013. NREL VI rotor blade: numerical investigation and winglet design and optimization using CFD. *Wind Energy* 17, 605–626.
- Mycek, P., Gaurier, B., Germain, G., et al., 2014a. Experimental study of the turbulence intensity effects on marine current turbines behavior. Part I: one single turbine. *Renew. Energy* 66, 729–746.
- Mycek, P., Gaurier, B., Germain, G., et al., 2014b. Experimental study of the turbulence intensity effects on marine current turbines behavior. Part II: two interacting turbines. *Renew. Energy* 68, 876–892.

- Nak, L., In, K., Chang, K., et al., 2015. Performance study on a counter-rotating tidal current turbine by CFD and model experimentation. *Renew. Energy* 79, 122–126.
- Robert, B., 2010. Mechanical Design of a Self-mooring Autonomous Underwater Vehicle (Master's thesis). Virginia Polytechnic Institute and State University, USA.
- Shen, W., Mikkelsen, R., Sørensen, N., et al., 2005. Tip loss corrections for wind turbine computations. *Wind Energy* 8, 457–475.
- Tedds, S., Poole, R., Owen, I., et al., 2011. Experimental investigation of horizontal axis tidal stream turbines. In: 9th European Wave and Tidal Energy Conference, Southampton, UK.
- Tongchitpakdee, C., Benjanirat, S., Sankar, L., 2005. Numerical simulation of the aerodynamics of horizontal axis wind turbines under yawed flow conditions. *J. Sol. Energy Eng.* 127, 464–474.
- Webb, C., Simonetti, J., Jones, P., 2001. Slocum: an underwater glider propelled by environmental energy. *IEEE J. Ocean. Eng.* 26, 447–452.
- Wenlong, T., Baowei, S., Zhaoyong, M., 2013. Conceptual design and numerical simulations of a vertical axis water turbine used for underwater mooring platforms. *Int. J. Nav. Archit. Ocean Eng.* 5, 625–634.
- Yuwei, L., Kwang-Jun, P., Tao, X., et al., 2012. Dynamic overset CFD simulations of wind turbine aerodynamics. *Renew. Energy* 37, 285–298.